Energy Conversions Associated With Magnetic Reconnection

S. Fadanelli, B. Lavraud, F. Califano, G. Cozzani, F. Finelli, M. Sisti

HAL Id: hal-03667198

https://amu.hal.science/hal-03667198

Submitted on 4 Jun 2022

Energy Conversions Associated With Magnetic Reconnection

S. Fadanelli[1,2] , **B. Lavraud[1]** , **F. Califano[2]** , **G. Cozzani[2,3]** , **F. Finelli[2]** , and **M. Sisti[2,4]**

[1]Institut de Recherche en Astrophysique et Planétologie, CNRS, UPS, CNES, Université de Toulouse, Toulouse, France, [2]Dipartimento di Fisica, Università di Pisa, Pisa, Italy, [3]Swedish Institute of Space Physics, Uppsala, Sweden, [4]Aix-Marseille University, CNRS, PIIM UMR, Marseille, France

Abstract We present theoretical and computational analyses of energy conversions in a magnetized collisionless plasma. We first revisit the theoretical approach to energy conversion analysis and discuss the expected correlations between the different conversion terms. We then present results from a Hybrid-Vlasov simulation of a turbulent plasma, focusing on the immediate vicinity of a reconnection site. Energy transfers are examined locally and correlations between them are discussed in detail. We show a good anticorrelation between pressure-driven and electromagnetic acceleration terms. A similar but weaker anticorrelation is found between the heat flux and thermodynamic work acting on internal energies. It is the departure from these anticorrelations that drives the effective changes in the species' kinetic and internal energies. We also show that overall energy gain or loss is statistically related to the local scale of the system, with higher conversion rates occurring mostly at the smallest local plasma scales. To summarize, we can say that the energization and de-energization of a plasma is the result of the complex interplay between multiple electromagnetic and thermodynamic effects, which are best taken into account via such a point-by-point analysis of the system.

1. Introduction

The dynamics of magnetized collisionless plasmas is characterized by the complex interplay of multiple energy conversion processes, spanning a wide range of scales and involving both thermal and nonthermal populations of different species. Various instabilities can trigger and regulate energy conversion in a plasma; among these, magnetic reconnection is one of the most studied when addressing plasma energization in the astrophysical context. During magnetic reconnection, magnetic field energy is converted into particles mechanical (i.e., bulk and internal) energy, yet the exact details on how energy is partitioned between kinetic and internal are still ambiguous (see the review of Yamada et al., 2016 and references therein).

Investigating kinetic and internal energy variations induced by reconnection is usually achieved by integrating the terms of the fluid energy density equations over some volume embedding the reconnection site and its close proximity. In this way, an "energy budget" for reconnection can be determined. This approach has been adopted successfully within the framework of magnetohydrodynamics (e.g. Birn et al., 2010; Birn & Hesse, 2010; Du et al., 2018; Hesse et al., 2011) as well as by considering plasma from a multifluid perspective (as in Aunai et al., 2011; Lu et al., 2018). A somewhat refined version of this analysis (such as in Hesse et al., 2018; Pucci et al., 2018; Wang et al., 2018; Yamada et al., 2015) identifies not a single box but many boxes to perform integration onto. By comparing energy budgets in boxes of different dimensions, in particular it is possible to determine a certain degree of spatial dependency in the energy repartition around the X line.

From the studies just mentioned, one common result is that in a reconnection site most of the incoming electromagnetic energy gets re-directed into the outflows, with the part transferred to plasma mainly ending up into disordered particle motion (i.e., the increase in internal energy density is dominant over that of kinetic energy). Another point of general agreement concerns the overall localization of energy exchanges. In the smallest integration boxes, that is, those covering the immediate surrounding of the X line (to about five ion inertial lengths from it), it is mostly electron energy (internal and kinetic) that increases. Instead, ions end up gaining most of the energy over larger domains, where electrons get decelerated and cooled (see Wang et al., 2018). Up to now, however, the idea of going beyond the "box approach" to quantify the precise

way in which energy conversions are locally interconnected with each other is a research line that seems to have been only marginally explored.

In the present work, instead of determining the overall energy budget we rather show how to study energy conversion processes through a local analysis of the neighborhood of a reconnection site. This is achieved by looking at statistical correlations of energy exchanges estimated in the framework of a multifluid description and evaluated point-by-point close to the X line. To this end, we simulate a turbulent magnetized proton-electron plasma with a hybrid Vlasov-fluid code and identify a reconnection site within it. This allows us to determine the spatial distribution of each term in the energy-density evolution equations for both protons and electrons. Then, two analyses are performed. First, by investigating correlations among all the terms involved we show how different processes contributing to energy conversion are interconnected. Second, a study of correlation of energy conversion terms with local system scales highlights how the local plasma scale is statistically linked with energy conversion rates.

The paper is organized as follows. In Section 2 we define the energy conversion rates, detailing our approach to energy conversion analysis. Section 3 introduces the code we used and how the numerical simulation is set. Section 4 contains the analyses, while discussions and conclusions are given in Section 5.

2. Theoretical Basis of Energy Conversion Rates

To distinguish ordered and disordered particle acceleration resulting from energy conversion processes, we describe the plasma using a multifluid framework, similarly to what was done in Birn and Hesse (2010) or Yang et al. (2017). Separating internal and kinetic energy density for each of the species, the equations describing the evolution of these energy densities are given by:

$$d_t K_s := \left[\partial_t + \mathbf{u_s} \cdot \nabla \right] K_s = -K_s \nabla \cdot \mathbf{u_s} - \mathbf{u_s} \cdot \nabla \cdot \mathbf{P_s} + q_s n_s \mathbf{u_s} \cdot \mathbf{E} \tag{1}$$

$$d_t U_s := \left[\partial_t + \mathbf{u_s} \cdot \nabla \right] U_s = -U_s \nabla \cdot \mathbf{u_s} - \mathbf{P_s} : \nabla \mathbf{u_s} - \left[\nabla \cdot \mathbf{Q_s} / 2 \right] \tag{2}$$

where the subscript "s" denotes the particle species, n_s is number density, $\mathbf{u_s}$ the fluid velocity, $\mathbf{P_s}$ the pressure tensor, $\mathbf{Q_s}$ the heat flux vector, $K_s := m_s n_s u_s^2 / 2$ and $U_s := 1 : \mathbf{P_s} / 2$ the kinetic and internal energy densities, respectively. Finally, q_s is the particle charge and m_s the mass.

Let us discuss in some detail what each term in these equations accounts for; that is, why we chose to write these equations in that form. In particular, since energy density variations in the streaming fluid, given by Lagrangian derivatives, always appear as the only left-hand side term, then all terms on the right-hand sides account for different effects that change energy densities in the streaming plasma, that is, in a given fluid element. First, energy densities can change because the fluid element has been compressed or expanded while keeping the same overall energy. The two terms $-K_s \nabla \cdot \mathbf{u_s}$, $-U_s \nabla \cdot \mathbf{u_s}$, account for these variations. Second, kinetic energy density may change because the fluid is accelerated/decelerated either by the presence of a pressure gradient, an effect taken into account by the term $-\mathbf{u_s} \cdot \nabla \cdot \mathbf{P_s}$, or because of an electric field, which is accounted for by $q_s n_s \mathbf{u_s} \cdot \mathbf{E}$. Third, changes in internal energy of a fluid element can be caused by converging/diverging velocity patterns, given by $-\mathbf{P_s} : \nabla \mathbf{u_s}$ and/or when incoming and outgoing heat fluxes are not balanced, i.e. when $-\nabla \cdot \mathbf{Q_s} / 2$ are nonzero. Furthermore, we remind that in multispecies plasma the electromagnetic field cannot impact directly the internal energy of any of the species when considered separately, but it can nonetheless increase or decrease the internal energy with respect to the plasma barycenter. This fact, for instance, is what requires us to insert another term in the equation for the evolution of internal energy when adopting a single-fluid plasma description. This "additional" term, sometimes known as the "dissipation" measure (see Zenitani et al., 2011), will not be present in our case, where energy exchanges are analyzed within a multifluid framework.

Even if the analysis presented here is similar to some mentioned in Section 1, in particular Birn and Hesse (2010) and Yang et al. (2017), yet let us underline the details in which our strategy is peculiar and different from these. First, note that since we focus on the local Lagrangian derivatives of K_s and U_s we need to identify the compression and decompression terms separately from the convective ones, not casted all together in the form of fluxes. Second, instead of computing the total thermodynamic work $-\nabla \cdot \left[\mathbf{u_s} \cdot \mathbf{P_s} \right]$

and $-\mathbf{u_s} \cdot \nabla \cdot \mathbf{P_s}$ as in Birn and Hesse (2010), or the total thermodynamic work and $-\mathbf{P_s} : \nabla \mathbf{u_s}$ as in Yang et al (2017), here we evaluate both $-\mathbf{u_s} \cdot \nabla \cdot \mathbf{P_s}$ and $-\mathbf{P_s} : \nabla \mathbf{u_s}$. Indeed, it is only by considering separately these two terms (acceleration and heating due to thermodynamic work) that we can retain information on the precise way by which internal and kinetic energy densities change along the streamlines, with U_s being acted upon by the surrounding velocity field and K_s being changed by local pressure derivatives. One last note concerns the impact of integration procedure on the relative importance of different energy conversion channels. In particular, since integrations over closed or periodic systems make the divergence vanish, a series of terms disappear from the space-integrated equations, and the terms that "survive" such integration may end up "coupling" with each other in a fashion that does not necessarily correspond to the point-by-point relation between energy conversion channels. This can be seen, for instance, in Yang et al. (2017) and Du et al. (2018), where box-wide integration implies that the heat flux is neglected and the integrals of thermodynamic work $-\mathbf{u_s} \cdot \nabla \cdot \mathbf{P_s}$ and $-\mathbf{P_s} : \nabla \mathbf{u_s}$ cancel out (indeed, these two terms sum up to the divergence term $-\nabla \cdot [\mathbf{u_s} \cdot \mathbf{P_s}]$). As our approach is based on a point-by-point analysis of heating and acceleration, no such "integral" coupling (resulting from vanishing integral terms) is taking place and all terms which appear in Equations 1 and 2 must be evaluated separately.

3. Code and Simulations

In order to perform the analysis just outlined, we focus on a reconnection site generated in a simulation of plasma turbulence which uses a hybrid Vlasov-Maxwell code (see Valentini et al., 2007). In particular, the code we use models the collisionless dynamics of a quasineutral, nonrelativistic ion-electron plasma by integrating the Vlasov equation for ions and assuming fluid electrons with an isothermal closure. The generalized Ohm's law we used includes the full Electron Magneto-Hydro-Dynamics (EMHD) regime. This hybrid approach offers a reasonable compromise between the computational time used and the level of accuracy obtained in describing the plasma dynamics, in particular at scales corresponding to the transition between fluid and ion-kinetic scales. It is worth noticing that the Eulerian approach used to advance in time the ion distribution function is characterized by a very low numerical noise even during the fully nonlinear regime (details on code and procedure for the integration of the Vlasov equation can be found in Mangeney et al., 2002; specifically, Pezzi et al., 2019 advocates for this code's reliability in energy transfer studies).

In the simulation considered here we adopt a 2D-3 V phase space geometry (two-dimensional in the spatial domain and three-dimensional in velocity space), denoting $\mathbf{e}_z$ the direction normal to the physical-space simulation box, $\mathbf{e}_x$ and $\mathbf{e}_y$ the in-box directions. Initially, the system is set into a uniform state with density n_0, magnetic field of intensity B_0 and directed along $\mathbf{e}_z$, and pressure P_0 is set equal to the magnetic energy density (i.e., the ratio of thermal to magnetic pressures—known as "plasma beta"—is one). Then, the system is perturbed by a sum of magnetic fluctuations resulting from a random phase combination of the first five Fourier modes of the box (corresponding to the larger wave lengths admitted by the system).

Throughout the code, all lengths and times are normalized, respectively, to the ion inertial length $d_i := \left[m_i c^2 / 4\pi n_0 q_i^2 \right]^{1/2}$ and the ion cyclotron period $\tau_i := m_i c / q_i B_0$ using the values n_0 and B_0 given at the initial time; mass unit is set to the ion mass m_i and charge unit is the ion charge q_i. To compute the temporal evolution of this system, the physical space $\left[0, L_x \right] \times \left[0, L_y \right]$, with periodic boundary conditions, is sampled by $N_x \times N_y$ grid points, while the velocity space, homogeneous with $\left[-v_{max} \leq v \leq v_{max} \right]$ in all directions, is discretized by $51 \times 51 \times 51$ points. For this run, we take $N_x = N_y = 3072$ and $L_x = L_y = 100\pi d_i$ and we set v_{max} to five times the thermal velocities (here equal to the ion Alfvén velocity $c_{Ai} := d_i / \tau_i = \left[B_0^2 / 4\pi n_0 m_i \right]^{1/2}$ due to initial conditions). From now on, all quantities will be expressed in code-normalized units.

We perform our analysis on a reconnection site that has developed in one of the self-generated current sheets within the domain. We focus on the local characteristics of the reconnection process, neglecting the global properties of the turbulence (like in Yang et al., 2017—the interested reader is referred to Califano et al., 2020; Franci et al., 2017; Hu et al., 2020 for a study of current sheets and turbulence in general). This simulation is meant to mimic the plasma turbulence that can be found in near-Earth space, notably at the magnetosheath close to the bow shock, where plasma beta is typically ≥ 1 and local compression of turbulent current sheets leads to reconnection (e.g., Vörös et al., 2017).
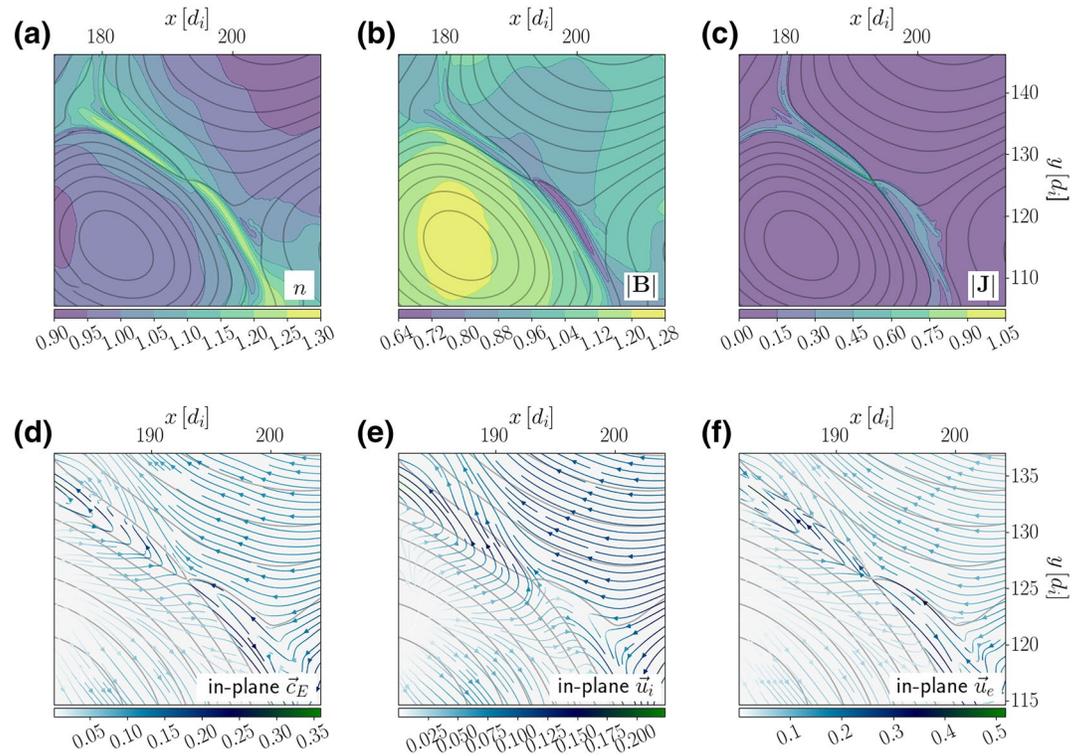
Figure 1. Simulation results of reconnection within a turbulent plasma, at time $170\,\tau_i$ of the simulation. The first row displays a wide perspective on the reconnection site (with frame-invariant quantities) while the second row shows a close-up of three in-plane velocities (all frame-dependent, evaluated in the reference co-moving with the X line as described in the text). Panel (a) number density (equal for ions and electrons), panel (b) magnetic field intensity, panel (c) absolute value of current density. Panel (d) in-plane components of the E × B drift. Panels (e and f) ion and electron in-plane velocities. In all panels, projected magnetic field lines are shown in black.

4. Spatial Patterns and Correlations Around a Reconnection Site

We analyze energy densities and energy conversion rates by looking at a current sheet that displays evident reconnection features, with an X line located at about $(193\,\mathrm{d_i}, 125.5\,\mathrm{d_i})$ at time $170\,\tau_i$. In Figure 1, top row, we show the large-scale context of this reconnection event by displaying the spatial pattern of number density, magnetic field intensity, and current density magnitude. An asymmetry between magnetic field strength in the two reconnecting regions (moving lower left to upper right, B_z passes from about unity to $\simeq 0.85$ while the in-plane field changes from $\simeq 0.27$ to $\simeq 0.12$) implies that the upper right separatrices are more bent than the lower left ones. Exhausts are recognizable as the regions where both number density and current density are enhanced.

4.1. Choosing the Reference Frame

By looking at Equations 1 and 2 we note that some terms are not frame-invariant. Therefore, the first step of the analysis of the energy conversion terms must be focused on the identification of a suitable reference frame. Here we set this reference frame as the one co-moving with the X line.

In order to find out the X line velocity $\mathbf{c}_x$, our choice is to follow the "spatio-temporal difference" (STD) method developed by Shi et al. (2006) to determine the velocity of any generic "magnetic structure" which is supposed to "evolve slowly" in time, that is, it is assumed that a frame exists in which the magnetic structure is stationary. In addition to having been applied to spacecraft measurements such as in Denton et al. (2016) or Genestreti et al. (2018), STD has been tested on numerical simulations by Denton et al. (2010; 2012) and proved quite accurate in providing structure velocity from "synthetic spacecraft" data. In particular, Murphy (2010), Murphy et al. (2015), and Juusola et al. (2018) have investigated the validity of assuming that the
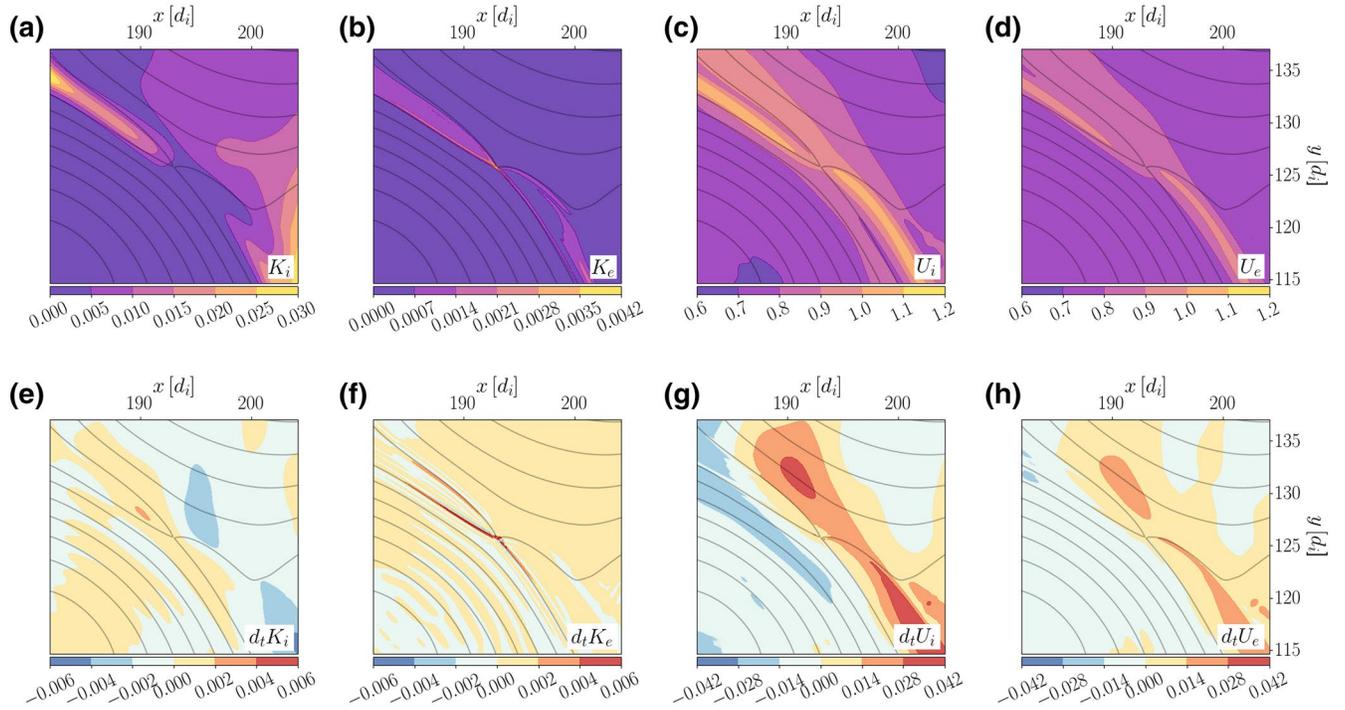
Figure 2. Ion and electron energy densities (top row) and their Lagrangian derivatives (bottom row) in the close proximity of the reconnection region, at time **t** = 170 τ_i. Panels (a and b) kinetic energy densities of ions and electrons respectively; panels (c and d) ion and electron internal energy density. Panels (e–h) Lagrangian derivatives of quantities in panels (a–d) respectively (calculated as sum of the right-hand side terms in Equations 1 and 2). In-plane projections of magnetic field lines are shown in black, and all terms have been evaluated in the reference frame where the X line is at rest, as described in the text.

X line moves with the velocity prescribed by STD, and all conclude that this is in excellent agreement with the X line velocity which is deduced by comparing successive times in the simulation output.

The STD method relies on the assumption that a frame exists in which the magnetic structure under study (here the X line) is at rest. Given this hypothesis, in any other reference one can write the relation $0 = \left[\partial_t + \mathbf{c}_x \cdot \nabla\right]\mathbf{B}$ and hence is provided immediately with the X line velocity:

$$\mathbf{c}_x = \left[\left[\nabla\mathbf{B}\right]^{-1}\right]^t \cdot \partial_t\mathbf{B} \qquad (3)$$

In the reference frame in which the X line is at rest, we are able to identify several typical reconnection signatures. This is shown in the bottom row of Figure 1. In particular, we find that the in-plane components of the electron velocity, ion velocity and E × B drift $\mathbf{c}_E := c\mathbf{E} \wedge \mathbf{B}/\mathbf{B}^2$ all show a stagnation point, which is located less than 1d$_i$ away from the X line for the electron velocity and E × B drift, and about 3d$_i$ downstream in the bottom-right part of the exhaust for the ion velocity (see panel 1e). This is consistent with the commonly accepted picture of (asymmetric) reconnection, for which the X line and stagnation point are not spatially coincident, as found by Cassak and Shay (2007), with the latter possibly located in the exhaust as in the case analyzed by Hasegawa et al. (2019). For all these reasons we deem this frame as appropriate for our analysis, and from now on we adopt it.

4.2. Spatial Patterns of Energy Densities and Their Lagrangian Derivatives

In this subsection we describe the patterns of energy densities and their Lagrangian derivatives around the reconnection site. These are shown in Figure 2. Discussing the kinetic and internal energy densities of ions and electrons in the vicinity of the reconnection region we intend to provide a detailed presentation of the reconnection site on which we will later perform statistical analyses. We remind that it is only using Lagrangian derivatives that one can identify where the fluid elements are energized or de-energized.

Let us first discuss the ion kinetic energy density, K_i, which increases in both exhausts, even if one of these clearly displays a stronger (more developed) ion jet (Figure 2a). To explain this asymmetry, let us remind that reconnection is sometimes unable to fully develop ion jets, in particular when constrained in a limited space. This was highlighted in the recent work of Sharma Pyakurel et al. (2019), that estimated 10–20d_i as the minimum exhaust length required for ion acceleration whenever reconnection is triggered in a small, periodic system. In our case, although the local boundary conditions are nonperiodic, we note that a similar scaling might apply. The fully developed ion jet (upper left in panel 2a) is hosted in an exhaust that runs straight for about 20d_i, while the slower outflow is bent and does not extend as much owing to larger scale constraints (nearby vortex dynamics). This asymmetric ion acceleration in the two outflows is consistently supported by the Lagrangian derivative of K_i (panel 2e), which shows that the ions in the lower-right outflow are locally experiencing a limited increase of K_i while those in the upper-left outflow get consistently accelerated.

On the other hand, electron kinetic energy density (panel 2b) and its Lagrangian derivative (panel 2f) show that electrons react to reconnection building up very localized regions of high velocity along the separatrices. The Lagrangian derivative of K_E (panel 2f) shows that acceleration takes place in the closest proximity of the X line, as expected in high guide-field reconnection (see for instance Pucci et al., 2018), and that accelerations and decelerations display a patchy structure (this is especially clear in the zoomed version of Figure S2 provided as Supplementary Information). This last pattern may be similar to what has been interpreted as a patchy electron diffusion region, and reported, albeit in cases with lower guide field, in spacecraft data (see Burch et al., 2018; Cozzani et al., 2019) and in simulations (see Swisdak et al., 2018).

The ion internal energy density displays an overall symmetric spatial distribution that peaks in the exhausts, in correspondence with local enhancements in number density (see panel 2c). High density due to pile up of material in the narrow exhausts and heating due to the release of magnetic energy are both well-known signatures from the literature. Values of $d_t U_i$ (panel 2g), however, are asymmetrically distributed in both the inflow and outflow regions, and generally uncorrelated to U_i. A possible explanation of this conundrum is found by the analysis of the in-plane ion flows (panel 1e). Indeed, a "diagonal" component of ion velocity shows that most of the upper left exhaust is characterized by plasma flow from high-U_i to low-U_i regions, the only exception being close to its lower separatrix. By such motion, one can explain both the negative $d_t U_i$ values observed for most of this exhaust and the thin region of positive $d_t U_i$ close to its lower separatrix.

In contrast to the net differences in kinetic energies, remarkable similarities are observed between U_i and U_E, as well as between $d_t U_i$ and $d_t U_E$. This is a consequence of the quasineutrality and of the isothermal electron assumptions, which prevent the development of specific electronic signatures around the reconnection site. Given this consideration, we shall not study electron internal energy, whose properties fall outside the scope of the present study.

Furthermore, we can compare the values of U_i and K_i in the outflows with the analytical-empirical expressions of the acceleration and heating trough reconnection by exploiting the following Equations:

$$K_{out} = \frac{mn_{out}u_{out}^2}{2} = n_{out} \frac{B_{L1} + B_{L2}}{8\pi} \frac{B_{L1}B_{L2}}{n_1 B_{L2} + n_2 B_{L1}} \tag{4}$$

$$U_{out} = \frac{3n_{out}T_{out}}{2} = n_{out}\left[\frac{U_1 B_{L2} + U_2 B_{L1}}{n_1 B_{L2} + n_2 B_{L1}} + \frac{3\alpha}{2} \frac{B_{L1} + B_{L2}}{4\pi} \frac{B_{L1}B_{L2}}{n_1 B_{L2} + n_2 B_{L1}} \right] \tag{5}$$

which are reported by Cassak and Shay (2007) and Phan et al. (2014), respectively. Subscripts "1" and "2" here indicate the two inflows, while "out" indicates quantities in the outflows. Subscript "L" for the magnetic field indicates that only the reconnecting component is considered and α is a dimensionless parameter.

In our case we can estimate B_{L1} between 0.10 and 0.15, B_{L2} between 0.25 and 0.30, and n_{out} between 1.05 and 1.10. Therefore, via Equation 4 we expect values between 0.01 and 0.02 for K_i in the exhausts, which is consistent with what is observed (especially in the upper left outflow, see panel 2a). Similarly, once taken $\alpha = 0.13$ as in Phan et al. (2014), U_i in the exhausts can be estimated between 0.96 and 1.12 from Equation 5, which is also consistent with the plot (see panel 2c). The large uncertainties, however, point out the difficulty in determining which "boundary" one should draw around this reconnection site, which is embedded

in larger-scale turbulence (see the Supplementary Information for a zoom-in plot of n, the in-plane B, K_i, and U_i, in the immediate surroundings of the X line). Such difficulties arising when a large-scale "energy budget" analysis is carried on, are removed completely by adopting the point-by-point approach of the present work.

4.3. Relations Between Energy Conversion Rates

Let us now focus on the causes of plasma energization, in particular on those processes leading to effective energy changes inside a fluid element. Such processes are described by the terms on the right-hand sides of Equations 1 and 2, apart from $-K_s\nabla\cdot\mathbf{u_s}$ and $-U_s\nabla\cdot\mathbf{u_s}$ which denote energy density variations due to compression and rarefaction. For the sake of clarity, from now on we will name "energy conversion rates" all those terms.

Figure 3 displays electromagnetic work ($+q_i n_i\mathbf{u_i}\cdot\mathbf{E}$ in panel 3d, $+q_E n_E\mathbf{u_e}\cdot\mathbf{E}$ in panel 3e) and pressure work ($-\mathbf{u_i}\cdot\nabla\cdot\mathbf{P_i}$ in panel 3a, $-\mathbf{u_e}\cdot\nabla\cdot\mathbf{P_e}$ in panel 3b) that accelerate/decelerate ions and electrons, alongside with the heat flux divergence ($-\nabla\cdot\mathbf{Q_i}/2$ in panel 3c) and thermodynamic work ($-\mathbf{P_i}:\nabla\mathbf{u_i}$ in panel 3f) associated with ion heating/cooling. Hence, effective energy changes result from the sum of the conversion rate terms which are plotted in panels 3a and 3d for K_i, 3b and 3e for K_E, 3c and 3f for U_i. The third row of Figure 3 displays the correlation of terms plotted in the first and second row, that is, the statistical occurrence of values in the parameter space defined by coupled energy conversion terms. Color of the dots in each of panels 3g, 3h, and 3i corresponds to the number of data points falling within each of the bins that cover the parameter space. The red lines superposed to all three distributions of the last row (panels 3g, 3h, and 3i) are obtained by performing linear regressions, setting by default that the line must pass through the origin and lowering noise by excluding data from within a circle of radius 0.0035 centered in the origin (this threshold has been found to be the lowest to allow good fitting). From now on, the result of linear regression indicates the "highest-confidence ratio" of coupled energy conversion rates.

Effective variations in kinetic energy are given by the sum of $-\mathbf{u_s}\cdot\nabla\cdot\mathbf{P_s}$ and $+q_s n_s\mathbf{u_s}\cdot\mathbf{E}$, accounting for acceleration due to thermodynamic and electric work, respectively. No effective change in K_s is possible, whenever force balance is in place, that is, whenever the system adjusts on the blue line in panels 3g, 3h, and 3i. According to Birn and Hesse (2010), the single-species force balance relation $\nabla\cdot\mathbf{P_s}=q_s n_s\left[\mathbf{E}+\mathbf{u_s}\wedge\mathbf{B}/c\right]$ should approximately hold nearly everywhere in the plasma. Hence we expect that energy conversion rates affecting K_s will generally sum up to zero.

By fitting data from the simulation, it appears that approximate balance of energy conversion rates is indeed observed, with a higher accuracy for electrons rather than for ions. Indeed, linear regression fits indicate that the highest-confidence ratio of $+q_s n_s\mathbf{u_s}\cdot\mathbf{E}$ over $-\mathbf{u_s}\cdot\nabla\cdot\mathbf{P_s}$ is -0.75 for ions and -1.19 for electrons, with the electron data set being slightly better correlated (the R^2 estimator, which is the square of correlation coefficient and approaches unity as the relationship between two variables approaches perfect linearity, scores 0.74 for ions and 0.96 for electrons). In the present example, despite small local departures from the diagonal, the two terms tend to compensate each other very precisely.

From Equation 2 we see that effective changes in internal energy density are achieved whenever the local thermodynamic work is not balanced by an appropriate heat flux divergence. As for variations in kinetic energy density, in this case also a correlation between energy conversion rates is to be expected: the values of $-\mathbf{P_s}:\nabla\mathbf{u_s}$ and $-\nabla\cdot\mathbf{Q_s}/2$ can be related to each other if the plasma behavior is polytropic and the noncompressional thermodynamic work is a finite percentage of the total, throughout all of the plasma. To explain this further, we introduce the polytropic index as $\gamma_s:=\left[d_t U_s\right]/\left[-U_s\nabla\cdot\mathbf{u_s}\right]$ (like in Pudovkin et al., 1997) and define the ratio $\delta_s:=\left[\mathbf{P_s}:\nabla\mathbf{u_s}-2/3\,U_s\,\nabla\cdot\mathbf{u_s}\right]/\left[\mathbf{P_s}:\nabla\mathbf{u_s}\right]$ (which is a sort of a "normalized" version of the Pi-D index by Yang et al. (2017)—in essence, δ_s accounts for the effects of anisotropy and off-diagonal terms in the pressure tensor and therefore it is expected to be typically much smaller than unity in most of the system). If the plasma is polytropic and noncompressional work accounts only for a small and rather constant percentage of the total, then:

$$\left(-\nabla\cdot\mathbf{Q_s}/2\right)/\left(-\mathbf{P_s}:\nabla\mathbf{u_s}\right)=\left[3\gamma_s-5\right]/\left[2-2\delta_s\right]-\delta_s \tag{6}$$
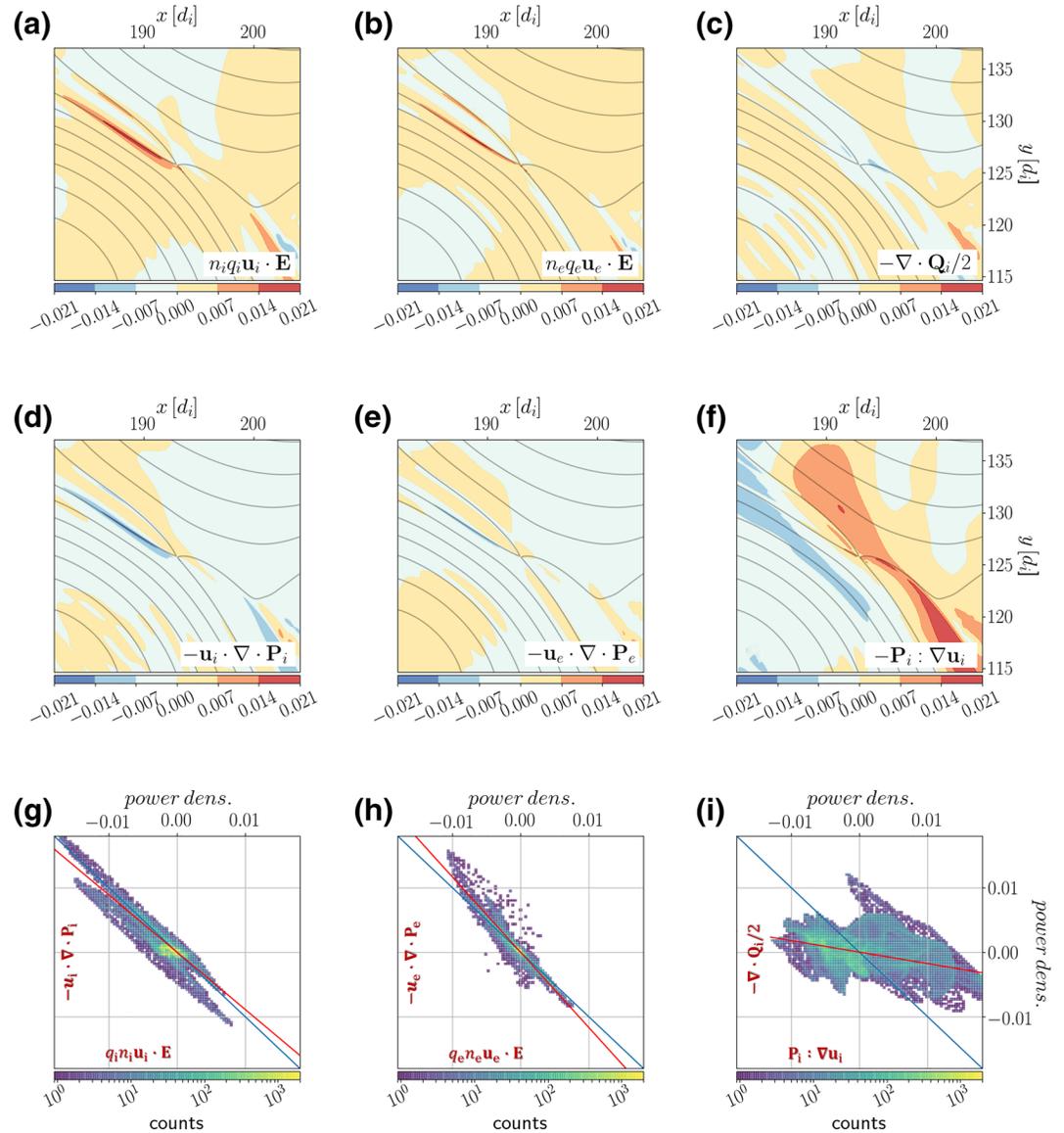
Figure 3. Comparison of ion energy conversion rates in the neighborhood of a reconnection region, with projected magnetic field lines in dark gray. First row, panels (a and b) work done by electromagnetic field on ions and electrons; panel (c) heating/cooling processes following from heat fluxes imbalance, for ions. Second row, panels (d and e) thermodynamic work to accelerate ions and electrons; panel (f) ion heating following from thermodynamic work. Third row: scatterplot histograms showing the correlation of the terms plotted in the two upper rows, panels (g and h) for ion and electron kinetic energies, panel (i) for ion internal energy. In other words, panels in the third row show the parameter space defined by coupled conversion rates, the color of each bin indicating for how many points of real space the values of energy conversion rates fall within the portion of parameter space covered by the bin. Red lines fit the most representative ratio in each sample, while blue lines are the diagonals that mark the frontier of no-net-energy-transfer that is, they separate overall energy gain (upper-right region) from energy loss (lower-left).

and therefore the ratio of $-\nabla \cdot \mathbf{Q}_s / 2$ over $-\mathbf{P}_s : \nabla \mathbf{u}_s$ must also be uniform throughout our reconnection neighborhood.

For example, if we consider the electrons in our simulation the isothermal assumption corresponds to $\gamma_e = 1$, while the absence of diagonal terms in the electron pressure tensor implies that the Pi-D term by Yang et al. (2017) is null everywhere, hence $\delta_e = 0$. Therefore, in our case $-\nabla \cdot \mathbf{Q}_e / 2$ must be perfectly balanced by $-\mathbf{P}_e : \nabla \mathbf{u}_e$ and no internal energy is effectively gained or lost in any compressions or decompressions
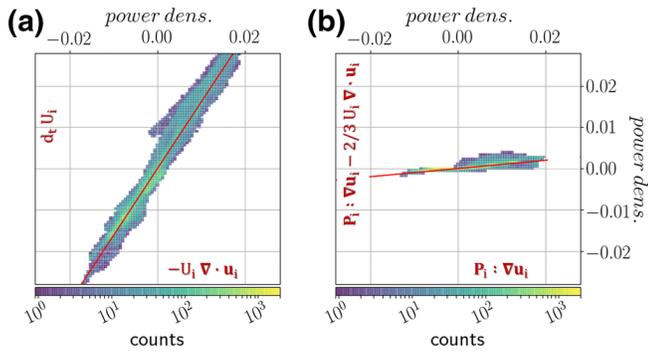
Figure 4. Evaluation of ratios γ_i and δ_i in the surrounding of the X line. The diagrams are scatterplot histograms showing point-by-point relationships of the numerator and denominator terms defining γ_i and δ_i (similar to panels in the third row of Figure 3). In other words, each bin covers some portion of the denominator/numerator parameter space, and its color is proportional to the number of points in real space for which denominator and numerator values fall within the bin. Red lines fit the most representative ratio in each sample.

of the electron fluid. Given the strong constraints posed by the closure equation on electron dynamics, however, we regard that previous case as not physically relevant and we don't draw from it any conclusion of sort.

Passing on to ions, we first note that γ_i and δ_i are well defined in the reconnection neighborhood, as one can note from Figure 4, their values being 1.61 and 0.10, respectively (with R^2 of 0.97 and 0.66). The small value of δ_i is overall consistent with the possibility of neglecting noncompressional work terms, while γ_i less than $5/3$ implies that plasma compression, as that which should accompany reconnection, ultimately results in internal energy gain. Even if only a weak correlation is observed when plotting $-\nabla \cdot \mathbf{Q}_i / 2$ versus $-\mathbf{P}_i : \nabla \mathbf{u}_i$ (see Figure 3i; R^2 likelihood is only 0.19), we still note that the retrieved δ_i and γ_i do predict quite well at least two of the overall trends in the plot. First, the observed slope of -0.18 agrees with the value of about -0.19 obtained inserting δ_i and γ_i in Equation 6. Second, the fact that most of the reconnection neighborhood exhibits an overall increase of U_i (most of the data points accumulate on the right and above the blue line) agrees with the heating expected to follow from plasma compression at the measured polytropic index. Given these two points of convergence, we suggest that the weak correlation observed in Figure 3i must not be attributed to some failure in having approximately uniform values of δ_i and γ_i close to the reconnection, but should rather be interpreted as the result of combining small and localized deviations from these near-constant behavior (possibly pointing at the complex fine structure of the reconnection neighborhood).
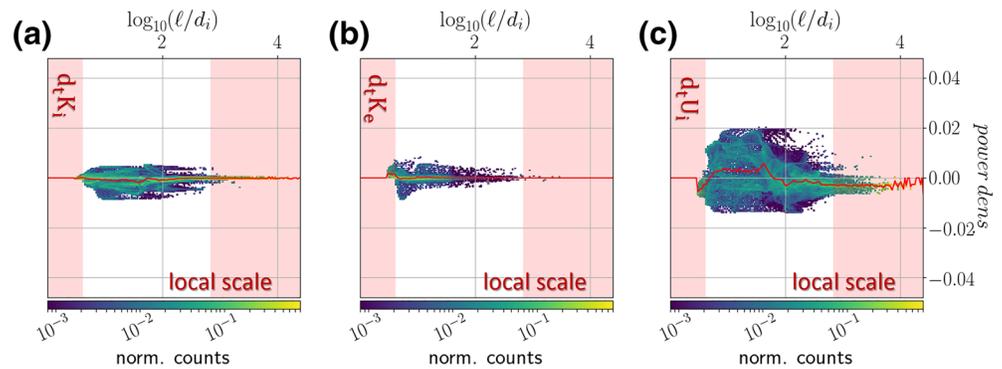
4.4. Local Scale and Energy Conversion Rates

An important aspect from Figure 3, as mentioned previously, is that coupled conversion rates tend in general to compensate each other, meaning that whenever one becomes strongly positive, the other tends to become negative, and vice-versa. Since effective energy gains or losses only occur whenever this counter-balancing is locally broken, in this last subsection we investigate statistically this behavior. We thus analyze how this breaking of the balance in the terms is linked to some scale of the system. The local scale we consider here is $\ell := n / |\nabla n|$, which quantifies the local fluctuation length of the plasma density n.

In Figure 5 we report the distribution of total energy conversion rates as a function of the characteristic length ℓ, in the surroundings of the reconnection site only (the zone taken is that depicted in Figures 2 and 3, reference frame change applied). This figure shows which is the percentage of points where the local scale is ℓ and energy conversion attains some given value. Furthermore, the red lines show the averaged energy transfer at each given scale. Intervals of scales with low statistics have been shaded red (less than 200 data points)

From panels 5a and 5b we find an overall balance between kinetic energy gains and losses through most scales (note that the per-scale averaged energy transfer indicated by the red line generally is very close to zero). For ion internal energy density, instead, the trend is a decrease at large scales and an increase at small scales (note that the red line of averaged energy transfer passes from positive to negative at about $100\,d_i$ in panel 5c).

4.5. Limitations

The hybrid model adopted here with kinetic ions and fluid electrons is particularly suited, also because of computational efficiency, for studying the physics across the ion cyclotron frequency. However, despite the inclusion of electron inertia capturing the full EMHD dynamics, the adopted isothermal closure, quasineutrality and in general the lack of the kinetic electron physics represents a limit for the electron energy conversion study. Indeed, effects at the electron scale (both spatial and temporal) are neglected, starting from all those driven by electron pressure anisotropy and all electron heating physics (for a review of

Figure 5. Scatterplot-like histograms of energy conversion rates (ordinates, logarithmic axis) at different local scales of the plasma (abscisses). Color scale is normalized for each vertical cut in the histograms i.e. yellow color highlights the most probable values attained by energy conversion rates at each scale along the abscissa, while blue color indicates the lowest frequency of observed values for each scale separately. Statistics is performed over the same neighborhood of the reconnection region depicted in Figures 2 and 3. Panels a and b refer to total conversion rates of kinetic energy, for ions and electrons. Panel c refers to total conversion rates of ion internal energy. Total conversion rates for electron internal energy, we remind, is identically zero at every scale because of the isothermal prescription implemented in the code. Red shading highlights data point statistics below 200.

electron-driven effects near reconnection sites see for instance Egedal et al., 2013). Another limitation is given by the two-dimensional geometry of the simulation considered, which constrains the overall system evolution. Two-dimensional setups, indeed, in many case lead to qualitatively similar results of fully three-dimensional simulations (see Wan et al., 2015 or Servidio et al., 2015) but in our case it might affect quantitatively the relative weight of the different phenomena at play in the turbulent dynamics (see Dahlin et al., 2015 discussing how the field-to-matter energy exchanges vary between two-dimensional and three-dimensional systems).

Also, the choice of a reconnection site which is generated and then remains constrained within a turbulent dynamics must be considered just as a different approach with respect to numerical works analyzing reconnection in a more laminar regime, in which the X line emerges from an initially prepared large-scale current sheet (Harris-sheet-like). These two approaches may not be directly compared, while both remaining valid with applicability to different plasma regimes. Our approach, for instance, impedes exhaust jets from fully developing and reaching the Alfvén speed (both for ions and electrons), as mentioned previously. It might also be responsible for the difference observed in ion and electron acceleration.

In any case, further work using this point-by-point approach should consider fully three-dimensional simulations, possibly using an even more accurate plasma model, or rely on satellite data.

5. Discussion and Conclusions

In the present work we have presented a novel approach to address the problem of energy conversion in a collisionless magnetized plasma and tested it by analyzing a reconnection site in a Vlasov-hybrid numerical simulation of plasma turbulence. Unlike most previous studies (several mentioned in the introduction), our approach is based on evaluating the exact, local Lagrangian derivatives of energy densities in order to follow the evolution of internal and kinetic energy relative to each fluid element. This approach allows us to study the spatial patterns of local energy conversion rates and, most important, their statistical correlations rather than providing a simple "energy budget" relative to some specific spatial region defined within the simulation.

This analysis specifically allows us to show that local kinetic energy variations in plasmas are usually small, since they require the breaking of the approximate force balance condition between pressure and electric force as pointed out by Birn and Hesse (2010). Moreover, we find that the average variation of internal energy in the dynamics reproduced by our hybrid code can be generally ascribed to an approximately polytropic behavior of the plasma, with corrections due to the noncompressional thermodynamic work. However,

large local deviations from this average trend point at the complex nature of local mechanisms leading to plasma heating and cooling.

The local character of the analysis performed also enables us to determine correlations of energy density transfers with the local scale of the system. In the close surroundings of the reconnection site, force balance tends to appear statistically at every scale, hence leading to an average conservation of kinetic energy densities. In the same region, a trend for large-scale decrease and small-scale increase is evident for ion internal energy density. Expanding the statistics, however, it appears that the largest values in energy conversion rates are observed around characteristic lengths of tens of d_i, and that on average these conversions result in an increase of plasma energy density.

The avoidance of volume integration in favor of a point-by-point analysis of energy conversion means, on the one hand, that no direct extrapolations may be made regarding global energy budgets. On the other hand, however, this approach also presents several major advantages with respect to the more traditional, space-integration-based "energy budget" method. First, not requiring volume integration makes the results independent of the procedure by which the integration volume is chosen so that the method is more robust. Second, not requiring integration implies that this procedure can be carried on in all such situations in which integration cannot be performed, such as for satellite data analysis. Hence, the method is easily portable. Third, by retaining values of all terms estimated locally at any time one can adopt a statistical approach to the energy conversion problem: the regions hosting energy conversions can be mapped in detail and the link between the energy conversion and the small-scale features of the system can be enlightened. This last characteristic of the procedure is particularly suitable to advance in the understanding of the nature of all localized energy conversion processes.

A natural further development would include the comparison with high resolution in situ data, as it has been done with measurements provided by MMS and Cluster within the frameworks of other energy transfer analyses (Chasapis et al., 2018; Eastwood et al., 2013; Ergun et al., 2018).

Data Availability Statement

All data is available online at the IRAP repository http://mms.irap.omp.eu/SID and at Cineca on the AIDA-DB (simulation UNIPI_TURB_2D). In order to access the metainformation and the link to the raw data, look at the tutorial at http://aida-space.eu/AIDAdb-iRODS. We thank E. Penou (IRAP) for help in data storage, and the reviewers for helpful questions and suggestions.

References

Aunai, N., Belmont, G., & Smets, R. (2011). Energy budgets in collisionless magnetic reconnection: Ion heating and bulk acceleration. *Physics of Plasmas*, *18*, 122901. https://doi.org/10.1063/1.3664320

Birn, J., Borovsky, J. E., Hesse, M., & Schindler, K. (2010). Scaling of asymmetric reconnection in compressible plasmas. *Physics of Plasmas*, *17*, 052108. https://doi.org10.1063/1.3429676

Birn, J., & Hesse, M. (2010). Energy release and transfer in guide field reconnection. *Physics of Plasmas*, *17*, 012109. https://doi.org/10.1063/1.3299388

Burch, J. L., Ergun, R. E., Cassak, P. A., Webster, J. M., Torbert, R. B., Giles, B. L., et al. (2018). Localized oscillatory energy conversion in magnetopause reconnection. *Geophysical Research Letters*, *45*, 1237–1245. https://doi.org/10.1002/2017GL076809

Califano, F., Cerri, S. S., Faganello, M., Laveder, D., Sisti, M., & Kunz, M. W. (2020). Electron-only reconnection in plasma turbulence. *Frontiers in Physiology*, *8*, 317. https://doi.org/10.3389/fphy.2020.00317

Cassak, P. A., & Shay, M. A. (2007). Scaling of asymmetric magnetic reconnection: General theory and collisional simulations. *Physics of Plasmas*, *14*, 102114. https://doi.org/10.1063/1.2795630

Chasapis, A., Yang, Y., Matthaeus, W. H., Parashar, T. N., Haggerty, C. C., Burch, J. L., et al. (2018). Energy conversion and collisionless plasma dissipation channels in the turbulent magnetosheath, observed by the magnetospheric multiscale mission. *The Astrophysical Journal*, *862*, 32. https://doi.org/10.3847/1538-4357/aac775

Cozzani, G., Retinò, A., Califano, F., Alexandrova, A., Le Contel, O., Khotyaintsev, Y., et al. (2019). In situ spacecraft observations of a structured electron diffusion region during magnetopause reconnection. *Physical Review 99*, 043204. https://doi.org/10.1103/PhysRevE.99.043204

Dahlin, J. T., Drake, J. F., & Swisdak, M. (2015). Electron acceleration in three-dimensional magnetic reconnection with a guide field. *Physics of Plasmas*, *22*, 100704. http://dx.doi.org/10.1063/1.4933212

Denton, R. E., Sonnerup, B. U. Ö., Birn, J., Teh, W.-L., Drake, J. F., Swisdak, M., et al. (2010). Test of methods to infer the magnetic reconnection geometry from spacecraft data. *Journal of Geophysical Research*, *115*, A10242. https://doi.org/10.1029/2010JA015420

Denton, R. E., Sonnerup, B. U. Ö., Hasegawa, H., Phan, T. D., Russell, C. T., Strangeway, R. J., et al. (2016). Motion of the MMS spacecraft relative to the magnetic reconnection structure observed on 16 October 2015 at 1307 UT. *Geophysical Research Letters*, *43*, 5589–5596. https://doi.org/10.1002/2016GL069214

Denton, R. E., Sonnerup, B. U. Ö., Swisdak, M., Birn, J., Drake, J. F., & Hesse, M. (2012). Test of Shi et al. method to infer the magnetic reconnection geometry from spacecraft data: MHD simulation with guide field and antiparallel kinetic simulation. *Journal of Geophysical Research*, *117*, A09201. https://doi.org/10.1029/2012JA017877

Du, S., Guo, F., Zank, G. P., Li, X., & Stanier, A. (2018). Plasma energization in colliding magnetic flux ropes. *The Astrophysical Journal*, *867*, 16. https://doi.org/10.3847/1538-4357/aae30e

Eastwood, J. P., Phan, T. D., Drake, J. F., Shay, M. A., Borg, A. L., Lavraud, B., & Taylor, M. G. G. T. (2013). Energy partition in magnetic reconnection in Earth's magnetotail. *Physical Review Letters*, *110*, 225001. https://doi.org/10.1103/PhysRevLett.110.225001

Egedal, J., Le, A., & Daughton, W. (2013). A review of pressure anisotropy caused by electron trapping in collisionless plasma, and its implications for magnetic reconnection. *Physics of Plasmas*, *20*, 061201. https://doi.org/10.1063/1.4811092

Ergun, R. E., Goodrich, K. A., Wilder, F. D., Ahmadi, N., Holmes, J. C., Eriksson, S., et al. (2018). Magnetic reconnection, turbulence, and particle acceleration: Observations in the Earth's magnetotail. *Geophysical Research Letters*, *45*, 3338–3347. https://doi.org/10.1002/2018GL076993

Franci, L., Cerri, S. S., Califano, F., Landi, S., Papini, E., Verdini, A., et al. (2017). Magnetic reconnection as a driver for a sub-ion-scale cascade in plasma turbulence. *The Astrophysical Journal Letters*, *850*(1). https://doi.org/10.3847/2041-8213/aa93fb

Genestreti, K. J., Cassak, P. A., Varsani, A., Burch, J. L., Nakamura, R., & Wang, S. (2018). Assessing the time dependence of reconnection with Poynting's theorem: MMS observations. *Geophysical Research Letters*, *45*, 2886–2892. https://doi.org/10.1002/2017GL076808

Hasegawa, H., Denton, R. E., Nakamura, R., Genestreti, K. J., Nakamura, T. K. M., Hwang, K.-J., et al. (2019). Reconstruction of the electron diffusion region of magnetotail reconnection seen by the MMS spacecraft on 11 July 2017. *Journal of Geophysical Research: Space Physics*, *124*, 122–138. https://doi.org/10.1029/2018JA026051

Hesse, M., Birn, J., & Zenitani, S. (2011). Magnetic reconnection in a compressible MHD plasma. *Physics of Plasmas*, *18*, 042104. https://doi.org/10.1063/1.3581077

Hesse, M., Liu, Y.-H., Chen, L.-J., Bessho, N., Wang, S., Burch, J. L., et al. (2018). The physical foundation of the reconnection electric field. *Physics of Plasmas*, *25*, 032901. https://doi.org/10.1063/1.5021461

Hu, A., Sisti, M., Finelli, F., Califano, F., Dargent, J., Faganello, M., et al. (2020). Identifying magnetic reconnection in 2D Hybrid Vlasov Maxwell simulations with convolutional neural networks. *The Astrophysical Journal*, *900*, 86. https://doi.org/10.3847/1538-4357/aba527

Juusola, L., Hoilijoki, S., Pfau-Kempf, Y., Ganse, U., Jarvinen, R., Battarbee, M., et al. (2018). Fast plasma sheet flows and X line motion in the Earth's magnetotail: results from a global hybrid-Vlasov simulation. *Annales Geophysicae*, *36*, 1183–1199. https://doi.org/10.5194/angeo-36-1183-2018

Lu, S., Pritchett, P. L., Angelopoulos, V., & Artemyev, A. V. (2018). Magnetic reconnection in Earth's magnetotail: Energy conversion and its earthward-tailward asymmetry. *Physics of Plasmas*, *25*, 012905. https://doi.org/10.1063/1.5016435

Mangeney, A., Califano, F., & Cavazzoni, C. (2002). A numerical scheme for the integration of the Vlasov-Maxwell system of equations. *Journal of Computational Physics*, *179*, 495. https://doi.org/10.1006/jcph.2002.7071

Murphy, N. A. (2010). Resistive magnetohydrodynamic simulations of X-line retreat during magnetic reconnection. *Physics of Plasmas*, *17*, 112310. https://doi.org/10.1063/1.3494570

Murphy, N. A., Parnell, C. E., & Haynes, A. L. (2015). The appearance, motion, and disappearance of three-dimensional magnetic null points. *Physics of Plasmas*, *22*, 102117. https://doi.org/10.1063/1.4934929

Pezzi, O., Yang, Y., Valentini, F., Servidio, S., Chasapis, A., Matthaeus, W. H., & Veltri, P. (2019). Energy conversion in turbulent weakly-collisional plasmas: Eulerian Hybrid Vlasov-Maxwell simulations. *Physics of Plasmas 26*, 072301. https://doi.org/10.1063/1.5100125

Phan, T. D., Drake, J. F., Shay, M. A., Gosling, J. T., Paschmann, G., Eastwood, J. P., et al. (2014). Ion bulk heating in magnetic reconnection exhausts at Earth's magnetopause: Dependence on the inflow Alfvén speed and magnetic shear angle. *Geophysical Research Letters*, *41*, 7002–7010. https://doi.org/10.1002/2014GL061547

Pucci, F., Usami, S., Ji, H., Guo, X., Horiuchi, R., Okamura, S., et al. (2018). Energy transfer and electron energization in collisionless magnetic reconnection for different guide-field intensities. *Physics of Plasmas*, *25*, 122111. https://doi.org/10.1063/1.5050992

Pudovkin, M. I., Meister, C.-V., Besser, B. P., & Biernat, H. K. (1997). The effective polytropic index in a magnetized plasma. *Journal of Geophysical Research*, *102*(A12), 27145–27149. https://doi.org/10.1029/97JA02447

Servidio, S., Valentini, F., Perrone, D., Greco, A., Califano, F., Matthaeus, W. H., & Veltri, P. (2015). A kinetic model of plasma turbulence. *Journal of Plasma Physics*, *81*, 325810107. https://doi.org/10.1017/S0022377814000841

Sharma Pyakurel, P., Shay, M. A., Phan, T. D., Matthaeus, W. H., Drake, J. F., et al. (2019). Transition from ion-coupled to electron-only reconnection: Basic physics and implications for plasma turbulence. *Physics of Plasmas*, *26*, 082307. https://doi.org/10.1063/1.5090403

Shi, Q. Q., Shen, C., Dunlop, M. W., Pu, Z. Y., Zong, Q.-G., Liu, Z.-X., et al. (2006). Motion of observed structures calculated from multi-point magnetic field measurements: Application to Cluster. *Geophysical Research Letters*, *33*, L08109. https://doi.org/10.1029/2005GL025073

Swisdak, M., Drake, J. F., Price, L., Burch, J. L., Cassak, P. A., & Phan, T.-D. (2018). Localized and intense energy conversion in the diffusion region of asymmetric magnetic reconnection. *Geophysical Research Letters*, *45*, 5260–5267. https://doi.org/10.1029/2017GL076862

Valentini, F., Travnicek, P., Califano, F., Hellinger, P. & Mangeney, A. (2007). A hybrid-Vlasov model based on the current advance method for the simulation of collisionless magnetized plasma. *Journal of Computational Physics*, *225*(1), 753–770. https://doi.org/10.1016/j.jcp.2007.01.001

Vörös, Z., Yordanova, E., Varsani, A., Genestreti, K. J., Khotyaintsev, Y. V., Li, W., et al. (2017). MMS observation of magnetic reconnection in the turbulent magnetosheath. *Journal of Geophysical Research: Space Physics*, *122*, 11442–11467. https://doi.org/10.1002/2017JA024535

Wang, S., Chen, L.-J., Bessho, N., Hesse, M., Yoo, J., Yamada, M., et al. (2018). Energy conversion and partition in the asymmetric reconnection diffusion region. *Journal of Geophysical Research: Space Physics*, *123*, 8185–8205. https://doi.org/10.1029/2018JA025519

Wan, M., Matthaeus, W. H., Roytershteyn, V., Karimabadi, M., Parashar, T., Wu, P., & Shay, M. (2015). Intermittent dissipation and heating in 3D kinetic plasma turbulence. *Physical Review Letters*, *114*, 175002. https://doi.org/10.1103/PhysRevLett.114.175002

Yamada, M., Yoo, J., Jara-Almonte, J., Daughton, W., Ji, H., Kulsrud, R. M., & Myers, C. E. (2015). Study of energy conversion and partitioning in the magnetic reconnection layer of a laboratory plasma. *Physics of Plasmas*, *22*, 056501. https://doi.org/10.1063/1.4920960

Yamada, M., Yoo, J., & Zenitani, S. (2016). Energy conversion and inventory of a prototypical magnetic reconnection layer. In W. Gonzalez & E. Parker (Eds.), *Book of magnetic reconnection* (Chap. 4; pp. 143–179). Switzerland: Springer International Publishing. https://doi.org/10.1007/978-3-319-26432-5_4

Yang, Y., Matthaeus, W. H., Parashar, T. N., Haggerty, C. C., Roytershteyn, V., Daughton, W., et al. (2017). Energy transfer, pressure tensor, and heating of kinetic plasma. *Physics of Plasmas 24*, 072306. https://doi.org/10.1063/1.4990421

Zenitani, S., Hesse, M., Klimas, A., & Kuznetsova, M. (2011). New measure of the dissipation region in collisionless magnetic reconnection. *Physical Review Letters*, *106*, 195003. https://doi.org/10.1103/PhysRevLett.106.195003